


Continental weathering and recovery from ocean nutrient stress during the Early Triassic Biotic Crisis

Jochen Knies^{1,2✉}, Jasmin Schönenberger¹, Horst Zwingmann³, Roelant van der Lelij¹, Morten Smelror¹, Per Erik Vullum⁴, Marco Brönnert¹, Christoph Vogt⁵, Ola Fredin⁶, Axel Müller ^{7,8}, Stephen E. Grasby^{9,10}, Benoit Beauchamp¹⁰ & Giulio Viola¹¹

Following the latest Permian extinction ~252 million years ago, normal marine and terrestrial ecosystems did not recover for another 5–9 million years. The driver(s) for the Early Triassic biotic crisis, marked by high atmospheric CO₂ concentration, extreme ocean warming, and marine anoxia, remains unclear. Here we constrain the timing of authigenic K-bearing mineral formation extracted from supergene weathering profiles of NW-Pangea by Argon geochronology, to demonstrate that an accelerated hydrological cycle causing intense chemical alteration of the continents occurred between ~254 and 248 Ma, and continued throughout the Triassic period. We show that enhanced ocean nutrient supply from this intense continental weathering did not trigger increased ocean productivity during the Early Triassic biotic crisis, due to strong thermal ocean stratification off NW Pangea. Nitrogen isotope constraints suggest, instead, that full recovery from ocean nutrient stress, despite some brief amelioration ~1.5 million years after the latest Permian extinction, did not commence until climate cooling revitalized the global upwelling systems and ocean mixing ~10 million years after the mass extinction.

¹Geological Survey of Norway, 7491 Trondheim, Norway. ²CAGE - Centre for Arctic Gas Hydrate, Environment and Climate, University of Tromsø, 9037 Tromsø, Norway. ³Department of Geology and Mineralogy, Kyoto University, Sakyo-ku, 606-8502 Kyoto, Japan. ⁴SINTEF Industry, 7034 Trondheim, Norway. ⁵Crystallography/FB5 Geosciences & MARUM, University of Bremen, 28334 Bremen, Germany. ⁶Department of Geoscience and Petroleum, Norwegian University of Science and Technology (NTNU), 7034 Trondheim, Norway. ⁷Natural History Museum, University of Oslo, 0318 Oslo, Norway. ⁸Natural History Museum, London SW7 5BD, United Kingdom. ⁹Geological Survey of Canada, Natural Resources Canada, Calgary T2L 2A7 AB, Canada. ¹⁰Department of Geoscience, University of Calgary, Calgary T2N 1N4 AB, Canada. ¹¹Department of Biological, Geological and Environmental Sciences, BiGeA, University of Bologna, 40126 Bologna, Italy. ✉email: jochen.knies@ngu.no

The causes of delayed recovery of devastated marine and terrestrial ecosystems following the latest Permian Extinction (LPE, ~252 Ma) are still debated^{1–3}. Possible events triggering the biotic crisis and prolonged recovery during the Early Triassic⁴ might have been episodic pulses of volcanisms and/or a CO₂-induced “hothouse” climate state with significant ocean redox perturbations that ultimately delayed the recovery of life^{1,3–5}. The Early Triassic biotic crisis (ETBC, ~252–247 Ma) corresponds to a relative palaeotemperature maximum albeit with short recovery episodes⁶ that was accompanied by an accelerated hydrological cycle and increased global weathering rates. Elevated continental weathering has been generally inferred from increased ⁸⁷Sr/⁸⁶Sr of marine carbonate^{7–9}, and anomalously high sediment fluxes during the Early Triassic^{10,11}. These inferences, however, are only derived from marine deposits and are thus indirect. The only direct evidence of enhanced continental weathering, although it stems from the direct aftermath of the LPE on terrestrial ecosystems, is from high-latitude paleosols (65°–85°S)¹², massive soil erosion at low-latitudes (equator)¹³, and specific lithium and magnesium isotope signatures derived from Paleo-Tethys marine deposits^{1,14,15} (Fig. 1). From these studies, enhanced continental weathering during the Early Triassic has been proposed as an effective mechanism for excessive nutrient supply to the oceans, thereby leading to marine eutrophication, anoxia, and ecological perturbations. Onshore NW Pangea, direct evidence for enhanced continental weathering is absent (Fig. 1) and knowledge of the relationship between chemical weathering intensity, ocean response, and climate and ecosystem recovery during the Early to Middle Triassic is effectively not available. Hence, a better understanding of the timing and spatial distribution of continental weathering during the ETBC is of importance for Earth system models to single out the role of CO₂ drawdown and marine anoxia during final climatic stabilization^{16,17}.

Remnants of continental basement weathering on NW Pangea in a warm and humid climate are reported beneath Pleistocene glacial deposits at a few localities in Fennoscandia^{18–23}. These terrestrial successions are significantly enriched in mature weathering products (i.e., kaolinite, gibbsite)^{18,20,21}. The exact timing of this kaolinitization, however, remains elusive except in southern Sweden and Denmark where overlying Jurassic–Cretaceous cover rocks provide minimum age constraints for basement weathering^{22,23}. Recently, Fredin et al.²⁰ showed that large regions of southwestern Fennoscandia have potentially been subjected to intense continental weathering in Late Triassic time



Fig. 1 Late Permian paleogeographic map. Paleogeographic map⁹⁷ and locations of studied sections from Norway (red star) and the Sverdrup Basin (blue star). Numbered yellow dots show areas with evidence of continental weathering from (1–3) Paleo-Tethys marine deposits^{1,14,15}, (4) massive soil erosion at mid-latitudes (Italy)¹³, and (5, 6) high-latitude paleosols (65°–85°S)¹². PTO Paleo-Tethys Ocean, NTO Neo-Tethys Ocean.

(ca. 220–200 Ma). Thus, evidence of enhanced continental weathering following the LPE is currently missing in Fennoscandia and elsewhere in NW Pangea (Fig. 1) implying that ocean response to continental weathering intensity and thus excessive nutrient supply can not be tested with the currently available data.

In this study, we characterize and directly date paleoweathering soils (saprolites) formed at the expense of crystalline basement rocks in northern Norway, along with two drill cores from offshore central Norway (Fig. 2). We report new data from chemically weathered rocks in crystalline granitoid basement occurring conformably below a 30 m (well 6408/12-U-01) to 170 m thick (well 6814/4-U-01; hereafter 6408 and 6814) Lower to Upper Jurassic sedimentary cover rocks offshore (Fig. 2)²⁴. Onshore, we studied Archean granitoids in a drill core (BH3) from Andøya, northern Norway, that are intensively kaolinitized and occur conformably below a 212 m thick Middle to Upper Jurassic (Bajocian–Kimmeridgian) sedimentary cover^{25–28}. We determined the age of weathering by K–Ar geochronology of authigenically formed K-bearing clay minerals separated from weathered basement rocks at all three investigated sites. We follow recent conceptual advances using K–Ar dating of clay as a valuable tool to date brittle fault rocks^{29–33} and weathering episodes²⁰. Conventional K–Ar dating was used instead of ⁴⁰Ar/³⁹Ar dating, since the latter is affected by ³⁹Ar recoil during sample irradiation³⁴ and requires non-standardized corrections, making it less suitable for dating fine-grained clay minerals. We couple this geochronologically constrained evidence for continental weathering with evidence for elevated marine productivity and ocean stratification by examining a continuous Lower to Middle Triassic deep water section off NW Pangea with the aim to constrain changes in nutrient utilization at mid-paleolatitudes (~40°N; Fig. 1). New nitrogen stable isotope ($\delta^{15}\text{N}$) data from Middle Triassic sections of Otto Creek, Sverdrup Basin, Canadian Arctic, are integrated with published Upper Permian to Lower Triassic bulk organic proxy data (TOC, $\delta^{13}\text{C}_{\text{org}}$, C/S ratio, $\delta^{15}\text{N}$) from Buchanan Lake³⁵ and Smith and Otto creeks, Sverdrup Basin^{5,36}. This new dataset helps to advance knowledge on the ocean response to enhanced continental weathering rates and ocean nutrient supply during “hothouse” climate conditions off NW Pangea. Analytical details are provided in the method section and supplementary online material.

Results and discussion

Evidence for continental weathering in central and northern Norway. The degree of weathering of crystalline bedrock from the studied off- and onshore wells was determined on unoriented powdered samples by X-ray diffraction (XRD) analysis, through major element composition using X-ray fluorescence (XRF) analysis and calculation of the chemical index of alteration (CIA)³⁷ and other weathering indices (CIW: Chemical Index of Weathering³⁸, PIA: Plagioclase Index of Alteration³⁹, and WIP: Weathering Index of Parker⁴⁰), in addition to mass-balance trends for major oxide depletion⁴¹ using Ti as an immobile index element⁴². XRD analysis of offshore wells 6408 and 6814 reveals a well-developed ~5–10 m thick saprolite layer beneath Mesozoic sediments etching into the Paleo- to Neoproterozoic granitoid and gneissic crystalline basement with kaolinite content approaching 70% in the bulk fraction (Fig. 3 and Table S1). Less than 30 wt% of the bulk fraction consists of primary minerals (K-feldspar, plagioclase) (Table S1). The kaolinite is well-ordered as shown by the sharply developed peak triplet at 4.0–4.5 Å⁴³ and may represent early diagenetic authigenesis^{44,45} (Fig. 3). Similarly, in situ kaolinitization of weathered Archean granitoids in Andøya BH3 is confirmed by the abundance of 32–36 wt% kaolinite in the bulk fraction with quartz being the dominant primary mineral

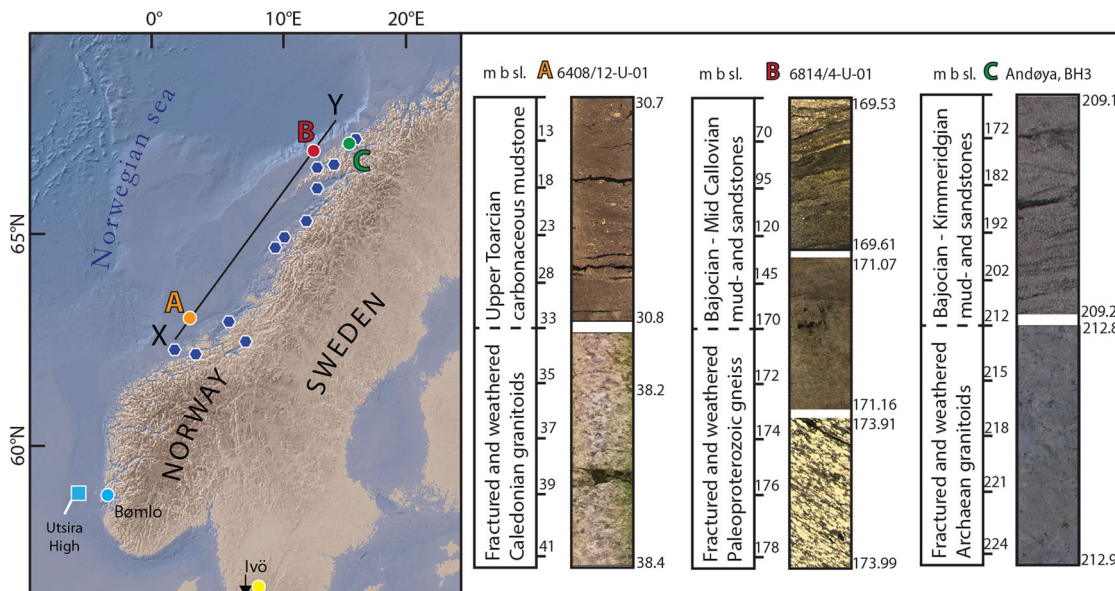


Fig. 2 Study area and site locations on- and offshore Norway. (Left) Map with studied wells 6408/12-U-01 (A), 6814/4-U-01 (B), and Andøya Borehole BH3 (C). The light blue square and circle indicate the location of the Late Triassic saprolite dated in Well 16/3-4 (Utsira High) and on the island of Bømlo²⁰, respectively. Yellow circle marks the Ivö location in southern Sweden²⁰. Blue hexagons: Location of Jurassic basins⁹⁸. Profile X-Y is schematically illustrated in Fig. 4a. (Right) Log, stratigraphy, and selected core images of wells 6408/12-U-01, 6814/4-U-01, and Andøya BH3 (mbsl. meter below seafloor).

(>50%) (Table S1). Mica clay minerals (i.e., illite) are a minor component (<11 wt%) in the bulk fractions. The Chemical Index of Alteration (CIA) in the weathered zone of all studied basement rocks increases upward from ~70 to ~96 (Table S2), thus constraining a gradual upward intensification of basement weathering as illustrated along an idealized SW-NE geological profile (Fig. 4a). Other weathering proxies (CIW, PIA, WIP) and the kaolinite content in the same samples corroborate this trend (Table S2). Furthermore, an A-CN-K plot (Al_2O_3 , $\text{CaO} + \text{Na}_2\text{O}$, K_2O) suited for granitoid basement rocks^{37,46,47} (Fig. 4b) confirms this advanced weathering trend for both offshore and onshore wells, with a gradual enrichment of relatively immobile Al and distinct kaolinitization towards the top of the weathering zone (Figs. 3, 4b)⁴⁸. Mass-balance trends in well 6814 support this interpretation of intense weathering by documenting distinct K- and Mg- (and moderate Fe-) depletion while Al remains largely constant⁴⁸ except it becomes progressively concentrated towards the altered zone at the top of the section (Fig. 4c).

Age of weathering. Dating weathering processes by absolute isotopic methods remains challenging and is mainly focused on dating supergene K-Mn oxides by K-Ar and $^{40}\text{Ar}/^{39}\text{Ar}$ methods⁴⁹. Due to the fact that weathering can indeed be part of a very long-lasting geological process, mostly integrated ages are reported⁴⁹. Weathering processes can result in rock alteration from the surface down and may be documented by inverted age profiles, with the oldest ages at the top surface and more recently weathered rocks in deeper parts of the weathering column yielding younger ages. K-Ar age dating of authigenically formed illite applied to constrain weathering processes is a new approach, originally introduced by Fredin et al.²⁰, and further discussed in the present study. This dating process relies upon different concepts than those of the classical mineral cooling models and Ar closure temperature⁵⁰. Instead of a simple cooling model, authigenic clays in weathering zones can, after their initial formation, reflect additional weathering and recrystallization episodes. Each subsequent weathering event might then partially or fully reset

the previously attained isotopic equilibrium between ^{40}K and radiogenic ^{40}Ar , resulting in a new “integrated K-Ar age”. Based on these complexities, the reported ages and errors of weathering events in the present study are larger than classical cooling isotopic ages and in the 2% range for authigenic illites (Table S3), but lower than the 7 to 18% errors for K-Ar ages of supergene K-Mn oxides⁴⁹.

Our new K-Ar ages in all three sites on- and offshore Norway range from 374.3 ± 7.6 Ma to 221.5 ± 5.9 Ma (Table S3). “Age vs. grain size” plots of the dated samples define inclined curves (Fig. 5), where the finest grain size fractions (<0.1, 0.1–0.4 μm) invariably yield the youngest ages, and the coarsest fractions (2–6, 6–10 μm) the oldest. All the eight ages of the 2–6 μm and 6–10 μm fractions define a cluster with a weighted mean age of 353.0 ± 2.3 Ma. The ages of the finest fractions (<0.1, 0.1–0.4 μm) range between 310 ± 6.8 and 221.5 ± 5.9 Ma. In Andøya BH3, not enough material could be separated from the limited core material to date the <0.1 μm fraction (Table S3).

Following recent conceptual advances in the K-Ar dating of clays in saprolitic material and brittle faults^{20,29–31}, we interpret the inclined curves of K-Ar ages in various grain size fractions as reflecting mixing between coarser protolithic or detrital illite/muscovite and the fine-grained authigenic K-bearing clay minerals that (neo)crystallized during deep weathering. Arguments in support of this interpretation, and thus of the reliability of the obtained geochronological results, derived from the characterization of the dated grain size fractions by XRD and TEM analysis.

XRD patterns display a dominance of characteristic triplets of kaolinite in the coarsest fractions (0.4–10 μm) at all sites (Figs. S1–4). This well-ordered nature of kaolinite is supported by its crystallinity index which was determined after both Hinckley (HI)^{51,52} and Liétard (R2)^{53,54}. For both approaches, the two coarsest, quartz- and feldspar-free fractions have an index of 0.9 (HI) and 1.0–1.1 (R2), which is characteristic of a high degree of ordering. This leads to the assumption that kaolinite may have crystallized at an early diagenetic stage, possibly under acidic conditions^{44,45}. In the coarsest fractions (2–6, 6–10 μm) at

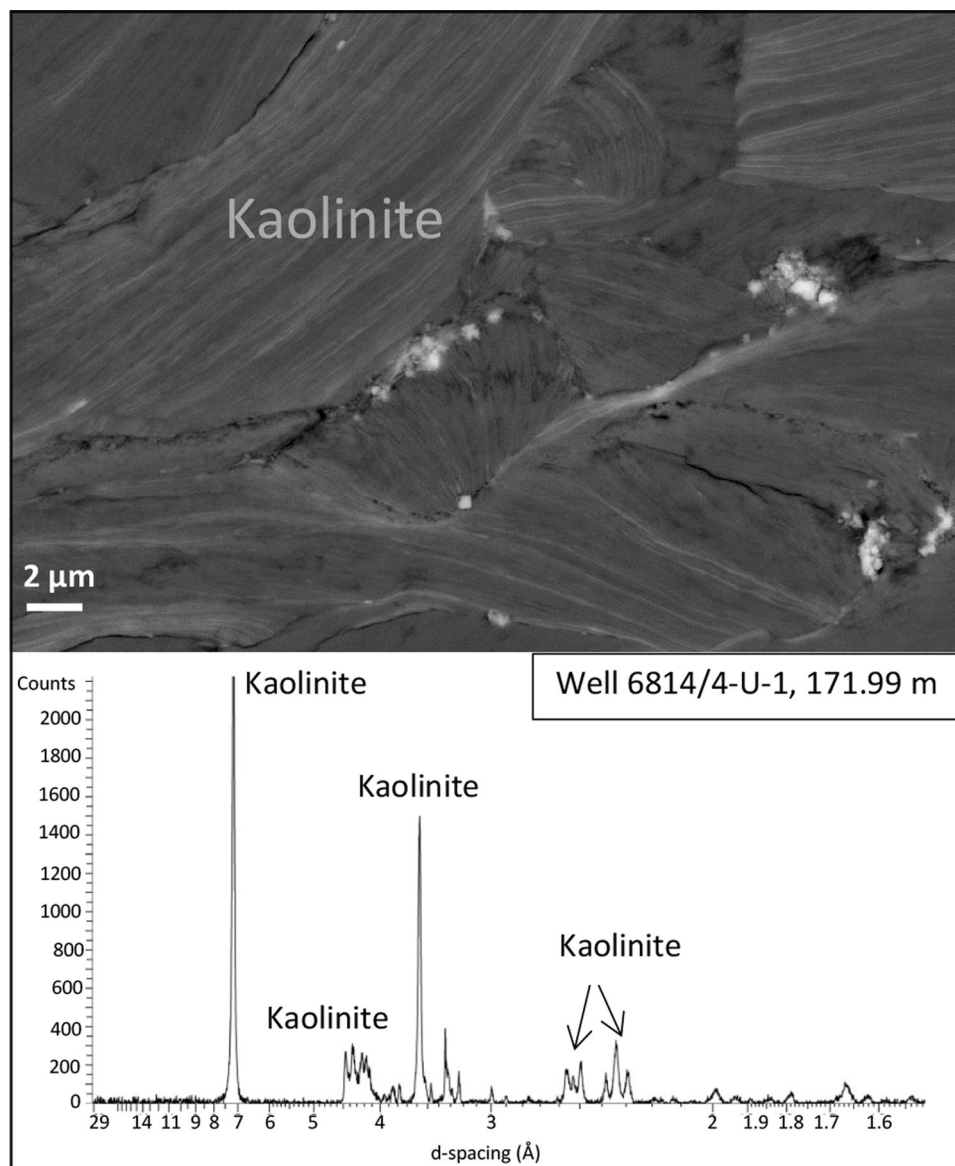


Fig. 3 SEM image and XRD characterization of weathered basement. SEM image and bulk XRD diffractogram of rock sample (171.99 m) in highly weathered basement from well 6814/4-U-01.

all sites, illite/muscovite is well-crystallized; its 10 \AA peak is sharply defined with a CIS-standardized FWHM of $<0.3 \text{ }^\circ 2\theta$. Along with the presence of K-feldspar in the coarsest fractions, an enrichment in protolithic (inherited) minerals is indicated in Andøya BH3 and well 6814 (Table S1 and Figs. S1, S3). In support of this interpretation for Andøya BH3 comes the illite polytype analysis. It confirms the presence of the well-crystallized $2M_1$ polytype at 2.8 \AA , interpreted as input from detrital muscovite, in both fractions with the oldest K-Ar ages⁵⁵, but its absence in the $0.4\text{--}2 \text{ }\mu\text{m}$ fraction, which yielded an intermediate K-Ar age (Fig. 5 and Figs. S3, S4). The $2M_1$ illite polytype is absent in the finer fractions in well 6408 as well (Fig. S2). The broadening of the smectite peak at 14 \AA towards the finer fractions ($0.4\text{--}2 \text{ }\mu\text{m}$) may suggest intercalation of minor amounts of illite in well 6408⁵⁶ (Fig. S2).

As to the finest fractions ($<0.1 \text{ }\mu\text{m}$, $0.1\text{--}0.4 \text{ }\mu\text{m}$), due to the lack of material, only material from well 6814 provided reliable XRD patterns, which indicate that kaolinite is the only clay mineral therein (Table. S1 and Fig. S1). Indeed, TEM analysis of the finest fractions confirms the presence of kaolinite with largely subhedral

to euhedral sheet morphologies (Fig. 6). Still, the presence of finely dispersed K-bearing particles is evident from the TEM EDS spectra in well 6814 (Fig. 6). Analogous to what was reported from kaolinite-rich Brazilian soils⁵⁷, these K-bearing phases may be interleaved in kaolinite crystals. Similarly, the finest fractions in well 6408 are largely composed of euhedral kaolinite minerals (Fig. 6). However, distinct K- and Mg-signals in the EDS spectra (Fig. 6) suggest that illite-intercalations within smectite contribute to the K-Ar ages of the finest fraction in well 6408. The finest fractions in Andøya BH3 contain authigenic illite with elongated euhedral particle edges (Fig. 6), which is also supported by the K signal in the EDS spectra.

The presence of K-bearing minerals within a matrix of largely subhedral to euhedral kaolinite minerals in the finest grain size fractions may suggest an authigenic crystallization during a more advanced stage of basement sapolitization. The unequivocal identification of authigenic illite in Andøya BH3 supports this inference. Still, the finest fractions may include inherited protolithic minerals or different generations of authigenic phases reworked during multiple stages of the weathering process. K-Ar

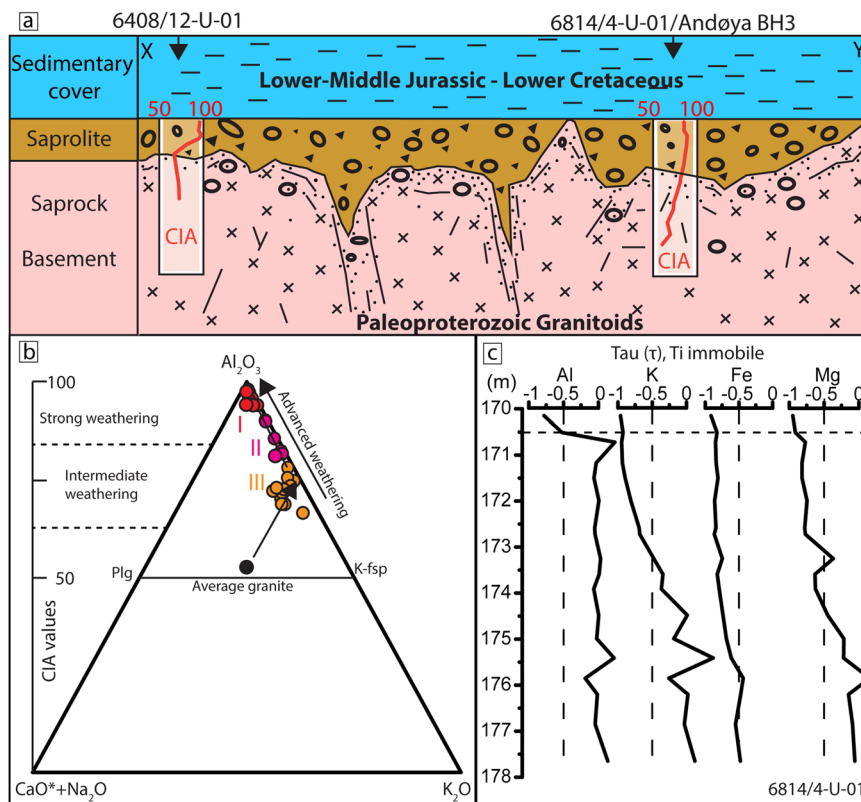


Fig. 4 Simplified geology and geochemical characterization of the weathered basement. **a** Simplified geological profile of fresh and weathered (saprolitic) crystalline basement overlain by Mesozoic sediments (not to scale). CIA chemical index of alteration profiles approaching values of 100 show the weathering zones in each basement section from the three studied locations. **b** CN-A-K (CaO + Na₂O, Al₂O₃, K₂O) plot with weathering indices (CIA), and weathering zonations I (red, strong weathering), and II-III (purple to orange, intermediate weathering) of granitoid bedrock according to Nesbitt and Young³⁷. Average granite composition (black dot) and its intermediate to strong/advanced weathering trends (arrows)^{46,47} support the inferred saprolitization of the studied granitoid basement below Mesozoic cover. **c** Mass balance with strain (tau, translocation) of well 6814/4-U-01 versus depth (in m) assuming immobile Ti. The stippled line indicates the transition between the weathered basement and Mesozoic cover.

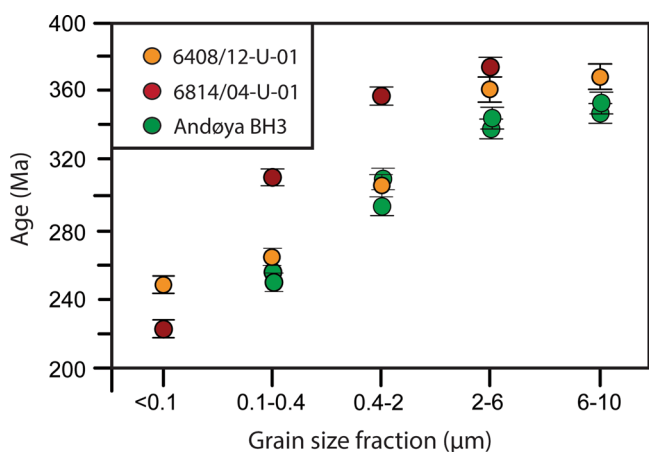


Fig. 5 K-Ar geochronology of weathered basement. K-Ar ages (Ma) versus grain size (µm) for the analysed samples from the highly weathered basement of offshore wells 6408/12-U-01 and 6814/04-U-01, as well as Andøya borehole BH3 onshore. K-Ar age errors (bars) are within 1σ uncertainties (see Table S3).

ages from the finest grain size fractions (<0.1 µm, 0.1–0.4 µm) should thus be considered as maximum ages, as studies from synkinematic brittle faults have shown^{29–31,58}. Hence, we follow the conceptual approach outlined by Fredin et al.²⁰ that the age of the finest fraction is taken as the best approximation of the

(maximum) age of the weathering episode. This is because the finest fractions contain the highest amount of authigenic K-bearing minerals and the least of potential contaminating mineral phases derived from the protolithic weathered rock^{20,29,30}.

A ca. 375–337 Ma age cluster (1) defined by seven ages of the coarsest fractions (2–10 µm) and one age in intermediate fraction (0.4–2 µm) (Fig. 7) corroborates the presence of well-crystallized illite (10 Å) and K-feldspar as well as the 2M₁ illite polytype (Figs. S1–S4), implying that this age cluster reflects a significant protolithic or detrital component from the respective source rocks. A second cluster (2) between 310 and 292 Ma is constrained by three ages by the intermediate (0.4–2 µm) fraction and one single age by the fine-grained (0.1–0.4 µm) fraction (Fig. 7). While the 2M₁ illite polytype was not identified in the intermediate grain fractions of well 6408 and Andøya BH3, well-crystallized illite peaks at 10 Å indicate a significant contribution from detrital components in this cluster (Figs. S2–S4). The ~310 Ma age in the kaolinite-rich matrix of the fine fraction (0.1–0.4 µm) in well 6814 is enigmatic and we interpret the K-Ar age as the result of mixed assemblages of authigenic and protholitic detrital K-bearing minerals interleaved within the kaolinite crystals. A third cluster (3) between 264 and 248 Ma is defined by 3 ages in the 0.1–0.4 µm fraction and one age in the finest fraction (<0.1 µm), permitting the calculation of a weighted mean age of 254.1 ± 2.6 Ma (Fig. 7). The presence of authigenic illite with elongated euhedral particle edges in an otherwise dominated matrix of kaolinite in this cluster (Fig. 6) may suggest

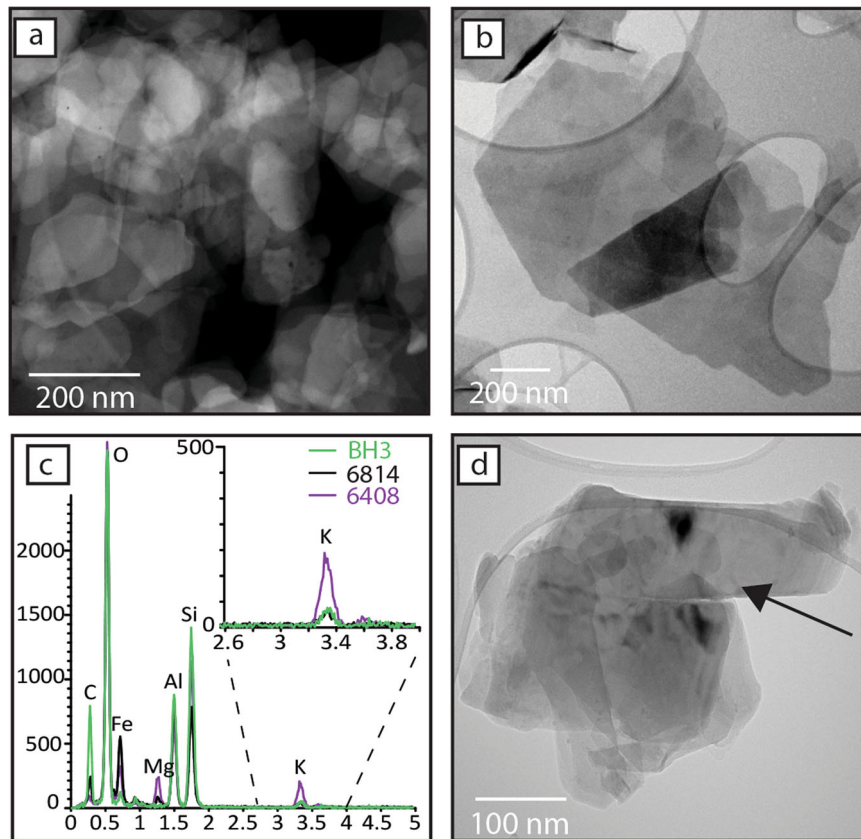


Fig. 6 Transmission electron microscopy (TEM) of the weathered basement. Photos and EDS spectra of K-bearing phases in the finest grain size fractions of the studied wells by TEM analyses: **a** Kaolinite in well 6814/04-U-01 and **b** 6408/04-U-01 with subhedral to euhedral morphologies. **c** EDS spectra showing evidence of K-bearing phases in the grain size fractions of all wells (purple: 6408/04-U-01; black: 6814/04-U-01; green: Andøya BH3). **d** Authigenic illite with elongated euhedral morphology (arrow) in Andøya BH3.

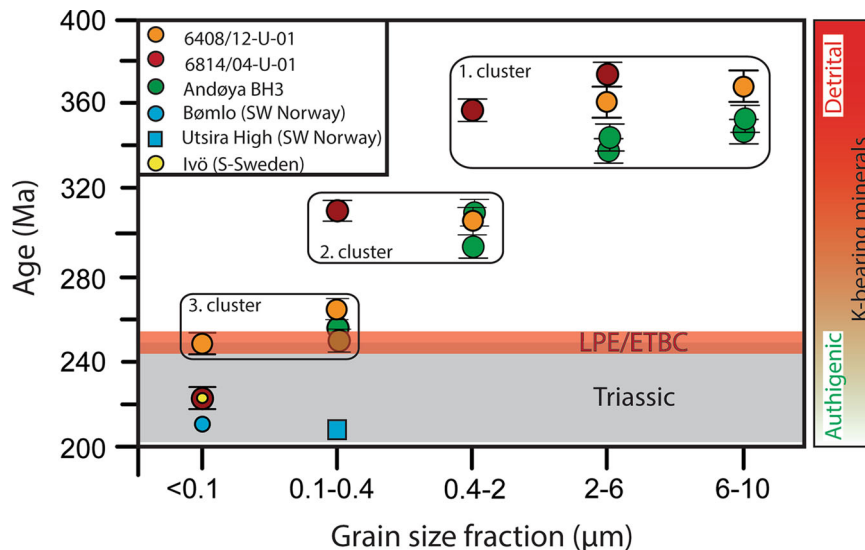


Fig. 7 Interpretation of K-Ar geochronological data. K-Ar ages in various grain size (μm) fractions with three different age clusters (1-3) as discussed in the main text. K-Ar age errors (bars) are within 1σ uncertainties (see Table S3). A single late Triassic age (221.5 Ma) in the finest fraction of well 6814/04-U-01 corroborates within error published results of weathered basements in southern Sweden (Ivö) (221.3 Ma) (yellow circle)²⁰. Published ages for the finest fraction in SW Norway (Bømlo, Utsira High) are shown by the light blue circle and rectangle²⁰. On the right, relative proportions of detrital and authigenic K-bearing minerals for each cluster are indicated.

a significant proportion of authigenically derived K-bearing minerals. The youngest age in the dataset (221.5 Ma) occurs in the finest fraction (<0.1 μm) of well 6814. This fraction is solely composed of kaolinite without clear evidence of the origin of the interleaved K-bearing particles and represents the most mature weathering stage of all studied samples.

Despite these remaining uncertainties on the origin of the K-bearing minerals, the verified presence of K-bearing authigenic minerals within a matrix largely dominated by highly mature weathering products suggests that the range of K-Ar ages in the third cluster (Fig. 7) provides the maximum age of saprolitization at all sites. The majority of ages for enhanced saprolitization of exposed crystalline basement between the Late Permian and Early Triassic (~254–248 Ma) is supported by inferences on a world-wide increase in sedimentation rates after the LPE¹⁰ that is attributed to a climate-driven increase in continental weathering^{1,14,15}. Increased sediment supply likely as a consequence of intense weathering as shown by the present study is recognized from northern Fennoscandia⁵⁹, Greenland and Spitsbergen⁶⁰ and Ural mountains⁶¹ during the Permian-Triassic transition. The single Late Triassic age (221.5 \pm 5.9 Ma) in the finest fraction (<0.1 μm) in well 6814 corroborate findings from southern Scandinavia (Ivö) where the weathered basement directly overlain by Upper Cretaceous sedimentary rocks yielded a maximum age of saprolitization of 221.3 \pm 7.0 Ma²⁰ (Fig. 7). Late Triassic ages (210–206 Ma) of saprolitization of a crystalline basement are also reported from Utsira High (North Sea), and from the island of Bømlo (SW Norway) (Fig. 7)²⁰. It remains debatable whether continental weathering intensified both in southern and northern Scandinavia already during Norian times (~227–209 Ma)⁶². Kaolinitic saprolites are inferred to have formed during warm and wet climatic conditions, preferably during Latest Triassic (Rhaetian) to Early Jurassic^{20,21,63}. However, increased humidity of the Boreal realm has already

been reported during Norian times^{64,65}. The single Middle Permian age (~264 Ma) in well 6814 remains enigmatic. A strong decline in seawater ⁸⁷Sr/⁸⁶Sr implies reduced continental weathering in central and northern Pangea, potentially fostered by dry climate and the absence of large orogens⁶⁶. Indeed, the widely developed Middle Permian evaporites and calcretes indicate a semi-arid to arid climate in the tropical regions of Pangea implying the reduced potential of weathering of the granitic continental crust^{67,68}. Whether the formation of weathering products can be linked to Emeishan flood volcanism during the Middle-Late Permian (~262 \pm 3 to 259 \pm 3 Ma)^{69,70} remains uncertain.

Continental weathering and recovery from ocean nutrient stress. The new K-Ar geochronological data provide—within the given 1 σ uncertainties (Table S3)—strong evidence for saprolitization and intense chemical weathering of NW Pangea during the Late Permian to Early Triassic (Fig. 8). Moreover, the near-complete transformation of the granitoid source rocks into authigenic kaolinite in two wells (Andøya BH3, 6408/12-U-01) with K-Ar ages between 249.5 to 248.1 Ma in the finest fraction (<0.1 μm), suggests intense weathering connected with a strong hydrological cycle under warm and humid climatic conditions during the ETBC (Fig. 8). The new evidence expands recent proxy (magnesium isotope) reconstruction for intensified chemical weathering of continental bedrock in the circum-Paleo-Tethys¹⁴ towards NW Pangea during the Early Triassic. To further test the ocean response to enhanced continental weathering and associated nutrient supply, we studied a complete Late Permian to Middle Triassic deep water record from Sverdrup Basin, Arctic Canada (Fig. 1), where a shale-dominated sediment sequence deposited in slope to distal shelf settings along the northwest margin of Pangea⁷¹. We examined new nitrogen isotope ($\delta^{15}\text{N}$)

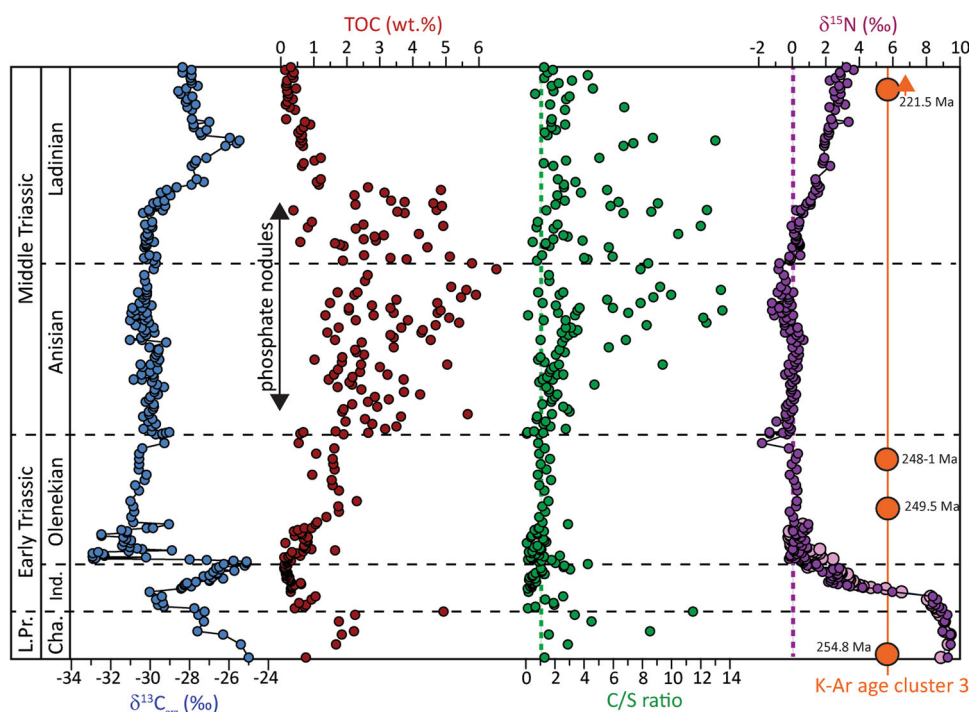


Fig. 8 Geochemical data from Otto Creek, Sverdrup Basin, Arctic Canada. Geochemical profiles show variations in carbon isotopes ($\delta^{13}\text{C}_{\text{org}}$), total organic carbon (TOC), carbon/sulfur (C/S) ratio, and nitrogen isotopes ($\delta^{15}\text{N}$), and are placed in relative time sequence. K-Ar ages of cluster 3 (see Fig. 7) across the LPE and the Late Triassic (221.3 Ma) are shown. The stippled vertical green line indicates C/S ratio -1 used to define relative changes in the redox state of the Sverdrup Basin. Prevalence of phosphate nodules are indicated⁵. Stratigraphic sub-units are marked by stippled lines. L.Pr. late Permian, Cha. Changhsingian, Ind. Induan.

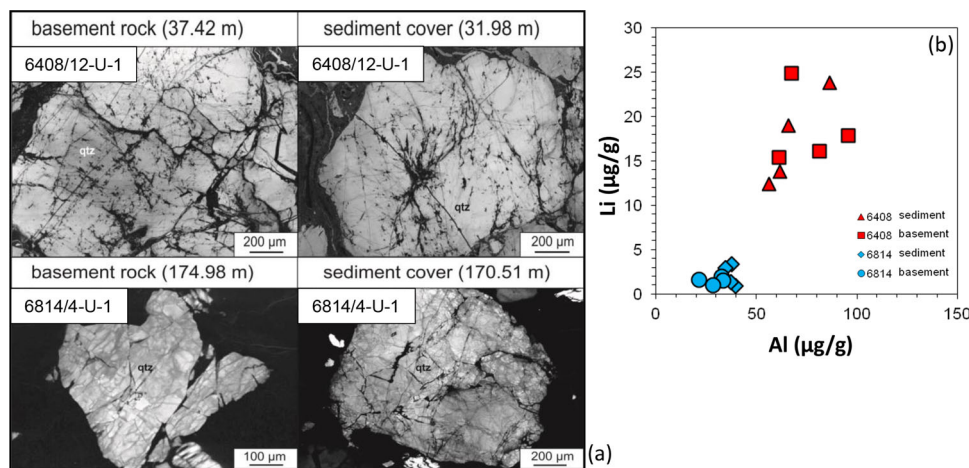


Fig. 9 Provenance assessment of weathered basement. **a** SEM-CL images of quartz grains from the weathered basement and early Jurassic sediment cover in well 6408/12-U-01 and 6814/4-U-01. Note the similarities of the grains suggesting that the Mesozoic sediment cover are derived locally from a weathered basement. **b** Concentration of Al versus Li (in $\mu\text{g g}^{-1}$) of quartz grains in the weathered basement and overlying Mesozoic sediments in wells 6814/4-U-01 and 6408/12-U-01. Note the correspondence between the weathered basement and overlying Mesozoic sediment cover in both wells.

data, along with key bioproductivity (TOC), redox-sensitive (C/S ratio), and nutrient (P) proxies (Fig. 8)^{5,35,36} to study the impact of chemical weathering intensity onshore on nutrient availability and, thus, to produce new constraints on primary productivity offshore NW Pangea.

Generally, the oceanic $\delta^{15}\text{N}$ signal depends on the isotopic composition of nitrate and the degree to which this inorganic nitrogen pool is utilized⁷². It records the combined isotopic signals of the inputs (mainly N_2 fixation) and outputs (mainly denitrification) of fixed nitrogen to and from the ocean^{72,73}. Previous studies have shown that records of $\delta^{15}\text{N}$ in sedimentary organic matter are useful to examine changes in the oceanic nitrogen cycle off NW Pangea across the Late Permian to Early Triassic crisis^{5,35,36,74}. The inference builds on the arguments that (1) there is little difference between the $\delta^{15}\text{N}$ of the original OM and diagenetically produced NH_4^+ ⁷⁵ (see methods for details) and (2) that postdepositional temperature changes exert negligible effects on sedimentary $\delta^{15}\text{N}$ ⁷⁶.

Knies et al.³⁵ reported that Late Permian high $\delta^{15}\text{N}$ values (>9‰) off NW Pangea (Fig. 8) are consistent with water-column denitrification in continental margin upwelling zones. These changes in oxygenation are largely controlled by the recycling of nutrients delivered from enhanced continental weathering and high organic productivity as documented by our dated weathering profiles onshore and elevated TOC values offshore (Fig. 8). The progressive $\delta^{15}\text{N}$ decline in the aftermath of the LPE has been interpreted as a decrease in nitrate availability in anoxic waters with a C/S ratio ≤ 1 (Fig. 8), shrinking the oceanic nutrient-N inventory that culminated in low ocean productivity (low TOC values) during the ETBC (Fig. 8)⁵. The related reduced nutrient supply to the surface caused significant nutrient stress in the photic zone with a prevalence of atmospheric N_2 -fixation as the major source for oceanic fixed nitrogen^{77,78}. The latter is documented by $\delta^{15}\text{N}$ values between $\sim 0\%$ and -1% during the Early Triassic (Fig. 8). The inferred ocean stagnation off NW Pangea is paralleled by a rising nutrient inventory in the deep sea. This pool of inorganic nutrients in the deep ocean during periods of anoxia/euxinia during the Early Triassic⁷⁹ was sustained by enhanced continental weathering as evidenced by our K-Ar ages of authigenically formed K-bearing minerals (Fig. 8) and elsewhere⁸⁰. Indeed, the finding of identical quartz grains in both lower Triassic saprolites and overlying Mesozoic marine sediments in wells 6408 and 6814 (Fig. 9) argues for the continuous

ocean supply of nutrients from an exposed and chemically weathered crystalline basement front either by marine or fluvial erosion during the ETBC. Regional tectonic uplift and denudation of basement rocks on NW Pangea during the Early-Middle Triassic⁸¹ provided sufficient (sub)aerial exposure to sustain basement weathering under “hothouse” climate conditions. Our observations agree with an inferred lower pole-to-equator temperature gradient of 2°C and higher global temperatures of $3\text{--}4^\circ\text{C}$ during the Early Triassic from climate system modeling^{3,82}. This timing of enhanced continental weathering also agrees with the proposed intensification of global weathering rates, and increased warming-driven river runoff inferred from rising $^{87}\text{Sr}/^{86}\text{Sr}$ isotopic variations⁸ (Fig. 10).

However, unlike the Paleo-Tethys, where direct evidence for reduced ocean redox conditions were likely caused by increased continental weathering, high productivity and ultimately marine eutrophication^{1,14,83}, the weathering on NW Pangea did not boost marine productivity in the adjacent Panthalassa Ocean as low TOC values indicate (Fig. 8)^{5,36}. Instead, the rapid rise in ocean surface temperatures (Fig. 10) and eventually thermal stratification⁶ counteracted the potential eutrophication, and thus fully anoxic conditions. Meyer et al.⁸⁴ suggested that the modeled estuarine-like circulation of the Paleo-Tethys acted as a nutrient trap implying a constant import of nutrient-rich deep waters with ongoing export of surface waters. The basinwide increase in nutrient levels with this nutrient-trapping ocean circulation may have caused widespread oceanic euxinia and hydrogen sulfide release to the atmosphere. In contrast, simulation results for the Panthalassa Ocean indicate a decline of Ekman-induced upwelling and thus reduced supply of nutrient-rich waters to the surface ocean during “hothouse” climate states³. Together with reduced cloud albedo and CO_2 -induced radiative forcing, the modeling results suggest that enhanced freshwater supply and warming of the polar sea surface led to a distinct thermo- and halocline, enhanced vertical stratification, and limited meridional overturning circulation^{3,82}, in agreement with preferred atmospheric N_2 fixation in surface water inferred from the nitrogen isotope data during the early Triassic (Fig. 10)^{5,35,36}.

Our new $\delta^{15}\text{N}$ data from Sverdrup Basin suggest that the predominance of diazotrophs as principle source for organic matter production offshore NW Pangea ended during the latest Anisian (~ 242 Ma). While organic-rich phosphatic black shales during Anisian times are still characterized by a ^{15}N content

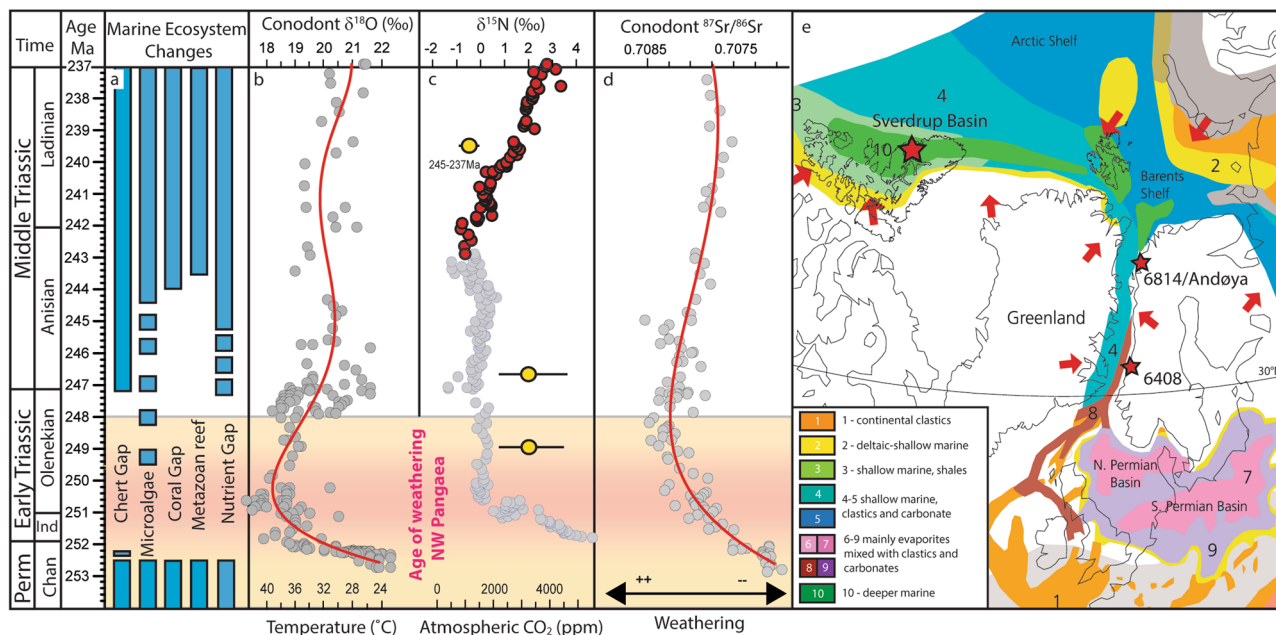


Fig. 10 Paleoclimatic and -ecological evolution during the Late Permian to Middle Triassic. **a** Marine ecosystem changes during the ETBC^{4,5}. **b** Tropical sea surface temperatures (SST) inferred from stable oxygen isotopes on conodonts⁸. **c** Composite nitrogen isotope ($\delta^{15}\text{N}$) record from Sverdrup Basin with previously published data in light blue circles^{5,35} and new data (Otto Creek) for this study highlighted in red. CO_2 data (yellow circles) from Royer⁹⁹. **d** Weathering variability inferred from strontium isotopes on conodonts⁸. **e** Paleogeographic reconstruction of NW Pangea during the early Triassic¹⁰⁰. The site locations of this study are marked by red stars. Arrows indicate potential pathways of detrital sediment discharge. Timing of intense continental weathering (~ 254 – 248 Ma) as revealed from K-Ar geochronology of authigenic K-bearing minerals in cluster 3 (Fig. 7) are indicated by beige horizontal gradients.

typical of newly fixed atmospheric N_2 ($\sim 0\%$) due to replenished surface nutrients with low N:P ratio⁵ (Fig. 8), the progressive rise of N-isotopes from -1% to $+3\%$ during the Ladinian (~ 242 – 237 Ma) (Fig. 8) suggests increasing upwelling of a partially denitrified water mass into the photic zone and subsequent utilization of various plankton groups. It marked the end of ocean stagnation with high nutrient inventories, as simulated for the LPE⁸⁵, however, not yet tested for the Early to Middle Triassic. Our data of gradual recovery from ocean nutrient stress since the latest Anisian corroborate a period of atmospheric CO_2 drawdown, reduced radiative forcing, and associated ocean cooling (Fig. 10) and reflect improved ocean mixing. With the upwelling of a partially denitrified, and thus $\delta^{15}\text{N}$ -enriched, water mass into the photic zone, residual nitrate gradually replaced N_2 -fixing cyanobacteria as the primary N-source utilized by marine phytoplankton that fueled the biological activity. This allowed the full recovery of marine ecosystems with common reptile- and fish-dominated communities from the end of the Anisian⁴ (Fig. 10).

In conclusion, our direct evidence of chemical weathering intensity of basement rocks onshore NW Pangea in the aftermath of the LPE supports modeling experiments suggesting that volcanic-induced warming and high pCO_2 stimulated continental weathering, and thus high nutrient supply to the ocean^{17,82}. The widespread anoxia⁷⁹, however, was not controlled by the surplus of nutrients and thus higher oxygen demand in the deep ocean due to higher export productivity, but rather by the stability of the thermal stratification of the ocean. The pool of additional nutrients from weathering continents was made available to massive organic matter production only when ocean mixing commenced again. Pre-LPE continental margin upwelling zones, however, were not established before the Early-Middle Ladinian, ca. 10 million years after the mass extinction, when deep water nutrients fuelled open-ocean marine productivity again.

Methods

Offshore and onshore material. Offshore well 6408/12-U-01 ($64^\circ 10' 13.3''\text{N}$, $08^\circ 44' 53.5''\text{E}$) recovered in total 33.3 m of Lower Jurassic (Late Toarcian) sedimentary rocks and weathered crystalline granitoid basement on the Trøndelag Platform, central Norway²⁴. The Jurassic sediments mainly consist of carbonaceous mudstone reflecting a transgression development from non-marine to lower shelf conditions. The underlying (unconstrained) granitoid basement is K-feldspar poor and intensively kaolinized and indicates exposure under warm and humid climate conditions²⁴. Well, 6814/04-U-01 ($68^\circ 39' 10.9''\text{N}$, $14^\circ 11' 08.9''\text{E}$) off the Lofoten/Vesterålen islands recovered in total 168.6 m of Middle to Upper Jurassic (Early/Middle Bathonian – Kimmeridgian) sediments and weathered crystalline gneiss basement²⁴. The gneiss in the basal part of the borehole (178.6–170.5 m) has been subjected to intensive kaolinite weathering and its parent composition is completely transformed into kaolinite at the boundary directly below the Jurassic sedimentary cover (Fig. 3). Unweathered gneiss at the base of the core is homogenous, foliated, gray-colored with small (< 5 mm) augen of micropertthitic feldspar and resembles Proterozoic mangeritic gneiss on the Lofoten-Vesterålen islands⁸⁶. Onshore, Andøya Borehole 3 (BH3) ($69^\circ 10' 32.7''\text{N}$, $16^\circ 0' 38.9''\text{E}$), recovered 225 m of Middle to Upper Jurassic (Bajocian–Kimmeridgian) sediments and weathered crystalline Archean granitoides²⁸. The Middle to Upper Jurassic unconformity is located at 176.4 m. The granitoides below 212 m of sedimentary cover have been subjected to intensive kaolinite weathering and are generally clay-rich (40%)²⁷.

X-ray diffractometry (XRD). Bulk mineral assemblages of dried, homogenized powder (< 20 μm particle size) and individual grain size fractions of wells 6408/12-U-01 and 6814/4-U-01 as well as Andøya BH3 (Tab. S1) were measured via X-ray diffraction (XRD) using a Bruker D8 Advance diffractometer with Cu K α radiation and a Lynxeye XE detector at the Geological Survey of Norway, Trondheim. XRD scans were carried out for 3 – $75^\circ 2\theta$ and a step size of 0.02° . Signal acquisition time was 1 s per step. The optical system was equipped with soller slits (2.5°) and fixed divergence and anti-scatter slits (0.6 mm). Full quantification of the mineral assemblage of the bulk fraction was conducted via the QUAX full pattern method at the University of Bremen⁸⁷. At NGU, mineral identification for different grain size fractions was carried out with Bruker's Diffrac.EVA 3.1 using ICDD's PDF4 Minerals as well as the Crystallographic Open Database. Quantification was performed with TOPAS and refined parameters included unit cell dimensions, sample displacement, preferred orientation as well as background coefficients. Limit of quantification and uncertainty is mineral-dependent, but commonly 1–2 wt% and 2–3 wt%, respectively. Illite crystallinity (Kübler Index) was determined from the full-width at half maximum (FWHM) of the 10 Å peak and standardized according to Warr^{88,89}.

X-ray fluorescence (XRF). Single samples (5cc) were analysed for major elements by using a PANalytical Axios sequential wavelength-dispersive XRF-spectrometer equipped with a 4 kW Rh X-ray tube at the Geological Survey of Norway, Trondheim. Loss on ignition (LOI) was determined after igniting 2–3 g finely-ground sample material for 1 h at 1000 °C. 4.200 ± 0.005 g $\text{Li}_2\text{B}_4\text{O}_7$ was mixed with 0.600 ± 0.005 g pre-ignited sample and fused to glass beads at 1200 °C in Pt95/Au5-crucibles. Accuracy was tested with certified reference materials (CRM). The analytical uncertainty is an element- and concentration-dependent, but usually better than 5% rel. (2 σ). Please refer to the raw data in Table S2.

Scanning electron microscopy (SEM) and catholuminescence. SEM investigations were carried out on carbon-coated thin sections of wells 6408/12-U-01 and 6814/4-U-01 using an LEO 1450VP analytical SEM at the Geological Survey of Norway in Trondheim. SEM was applied to document kaolinite in a weathered basement (Fig. 3) and the microstructure of quartz in basement samples by backscattered electron (BSE) imaging (Fig. 9). SEM-catholuminescence (SEM-CL) images of quartz were obtained with a Centaurus BS Bialkali CL detector attached to the LEO 1450VP analytical SEM. The applied voltage and current were the same as for the SEM investigations (20 kV, ~2 nA). The Bialkali tube has a CL response range from 300 (violet) to 650 nm (red). The detector sensitivity peaks in the violet spectrum range around 400 nm. SEM-CL images were collected from one scan of 43 s photo speed and a processing resolution of 1024×768 pixels and 256 gray levels.

Transmission electron microscopy (TEM). Transmission electron microscopy (TEM) studies were conducted on all three studied wells at NTNU (Fig. 6). The sample powders were dispersed in isopropanol, ultrasonicated for 5–10 min, before a droplet was transferred to a holey, carbon-coated Cu TEM grid. TEM was performed with a double Cs aberration-corrected cold FEG JEOL ARM 200FC, operated at 200 kV. This TEM is equipped with a 100 mm^2 (covering 0.98 sr solid angle) Centurio detector for energy-dispersive X-ray spectroscopy (EDS). EDS was performed by the acquisition of two-dimensional maps in scanning transmission electron microscopy (STEM) mode. The Cliff-Lorimer equation, by employing theoretical k-factors, was used for quantification of the chemical composition. Error estimates for the EDS quantifications are not included since the error bars due to counting statistics are negligible, while the systematic errors due to X-ray re-absorption are sample thickness and element dependent and vary from one location to another.

Laser ablation inductively coupled plasma mass spectrometry (LA-ICP-MS). Trace element concentrations in quartz were determined by LA-ICP-MS (Fig. 9). The samples were prepared as surface-polished, 300- μm -thick sections mounted on standard glass slides. The analyses were undertaken with a double-focusing high mass-resolution sector-field (HR-SF) ICP-MS, model ELEMENT XR from Thermo Scientific, located at the Geological Survey of Norway in Trondheim. The instrument is linked to a 193 nm New Wave UP193FX ESI excimer laser probe. The laser parameters are provided in Table S4. A continuous raster or line ablation was applied. The carrier gas for transport of the ablated material to the ICP-MS was He mixed with Ar. The isotope ^{29}Si was used as the internal standard, applying the stoichiometric concentration of Si in quartz. External standards applied for calibration are given in Table S4. Certified, recommended, and proposed values for these reference materials were taken from ref. ⁹⁰. Each measurement comprised 15 scans of each isotope. An Ar blank was run before each reference material and sample measurement to determine the background signal. The background was subtracted from the instrumental response of the reference material/sample before normalization against the internal standard in order to avoid the effects of instrumental drift and memory between sample measurements. A weighted least squares regression model, including several measurements of the reference materials, was used to define the calibration curve for each element. Ten sequential measurements of the BAM No.1 SiO_2 quartz glass were used to estimate the limits of detection (LOD) which were based on $3 \times$ standard deviation (3σ) of the ten measurements.

K-Ar dating of sapolite illite. All analytical details for the present study have been described by refs. ^{20,30}. K-Ar dating was optimally performed on five clay size fractions (<0.1, <0.4, <2, <6, and 6–10 μm). For samples of wells 6408/12-U-01 (all fractions) and 6814/4-U-01 (<2 μm), K-Ar-analysis were conducted at CSIRO, Australia. K-analysis was done by atomic absorption spectrometry (AAS, Varian Spectra AA 50). For Ar analysis by noble gas spectrometry, sample splits were loaded into clean Mo foil, weighed and subsequently pre-heated to 80 °C overnight to remove moisture, and reweighed using a Mettler AT20 balance. The measured dry weight was used in the K-Ar age calculation. Once loaded into the gas purification line, the samples were pre-heated under vacuum at 80 °C for several hours to reduce the amount of atmospheric Ar adsorbed onto the mineral surfaces during sample handling. Argon was extracted from the separated clay mineral fractions by fusing samples within a vacuum line with an online ^{38}Ar spike pipette. The isotopic composition of the spiked Ar was measured with a high sensitivity online VG3600 mass spectrometer. The ^{38}Ar spike was calibrated against standard biotite GA1550⁹¹. Blanks for the extraction line and mass spectrometer were

systematically determined and the mass discrimination factor was determined periodically by air shots (Table S5).

K-Ar analysis of all fractions of Andøya BH3 and fractions 2–6, <0.4, and <0.1 μm of well 6814/4-U-01 was conducted at the Geological Survey of Norway following protocols outlined in ref. ³¹. Potassium was determined by fluxing clay samples in Li-tetraborate and digesting the resulting glass in HNO_3 prior to analysis on a Perkin Elmer 5110DV ICP-OES. Argon concentrations were determined by weighing samples on a Mettler-Toledo XP26DR microbalance, and fusing in a Pond Engineering furnace at 1400 °C. The evolved gas was spiked with pure ^{38}Ar , calibrated using HD-B1^{92,93} and purified using a combination of SAES-GP50 (ST101) getters and a Titanium Sublimation Pump. Argon isotope intensities were measured using an IsotopX NGX multicollector noble gas mass spectrometer. Although the calibration standards used at NGU (HD-B1) are different from CSIRO (GA1550), 22 analyses of GA1550 at NGU yield a weighted mean age of 98.55 ± 0.07 Ma (MSWD = 1.18), which compares favorably to the published age of 98.5 ± 0.5 Ma⁹⁴. The calibrations between both laboratories are thus comparable.

All K-Ar ages were calculated using ^{40}K abundance and decay constants recommended by Steiger and Jäger⁹⁵. The pooled error of duplicate K determination on all samples and standards is better than 2%, whereas the error for Ar analyses is below 1%. The age uncertainties take into account the errors during sample weighing, $^{38}\text{Ar}/^{36}\text{Ar}$ and $^{40}\text{Ar}/^{38}\text{Ar}$ measurements, and K-analysis. K-Ar age errors are within 1σ uncertainties.

Stable nitrogen isotopes. For the stable nitrogen isotope analyses, we studied a composite section of (1) Late Permian from Buchanan Lake³⁵, (2) Early Triassic from Smith Creek (Smithian stratotype)⁵, and (3) Middle Triassic from Otto Creek (this study). The three locations from Sverdrup Basin, Arctic Canada have similar shale-dominated sedimentation in slope to distal shelf settings at mid-paleolatitudes (~40°N)⁷¹. Total N and $\delta^{15}\text{N}_{\text{tot}}$ were analysed on homogenized sub-samples by elemental analyser isotope ratio mass spectrometry (EA-IRMS) on an ANCA-GSL/20-20 system (Europa Scientific, Crewe, UK). Approximately 20% of the samples were analyzed in duplicate with a mean standard deviation of 0.16‰. $\delta^{15}\text{N}_{\text{tot}}$ data are reported as standard δ -values per mil (‰ vs. air). A KOB-CO₂ treated aliquot in pre-selected samples measures the amount of inorganic nitrogen (IN) and its isotopic signature ($\delta^{15}\text{N}_{\text{inorg}}$)³⁵ representing the amount of NH_4^+ fixed within the clay lattice⁹⁶ (Table S6 and Supplementary Data 1). We observe nearly identical $\delta^{15}\text{N}_{\text{inorg}}$ (mean 3.07‰) and $\delta^{15}\text{N}_{\text{tot}}$ (mean 2.79‰) values with a covariance of 0.95 and a significant covariation between TOC and TOC/IN ratio ($R^2 = 0.8$) suggesting an organic origin for the IN. All geochemical proxy data for the middle Triassic Otto Creek profile are reported in Table S7 (Supplementary Data 2).

Data availability

Underlying data for the main manuscript figures is included in the text and provided as an excel file in source data or can be accessed at <https://doi.org/10.6084/m9.figshare.19738858.v2>.

Received: 29 October 2021; Accepted: 16 June 2022;

Published online: 15 July 2022

References

- Zhang, F. et al. Multiple episodes of extensive marine anoxia linked to global warming and continental weathering following the latest Permian mass extinction. *Sci. Adv.* <https://doi.org/10.1126/sciadv.1602921> (2018).
- Kidder, D. L. & Worsley, T. R. Causes and consequences of extreme Permian-Triassic warming to globally equable climate and relation to the Permian-Triassic extinction and recovery. *Palaeogeogr. Palaeoclimatol. Palaeoecol.* **203**, 207–237 (2004).
- Winguth, A. M. E., Shields, C. A. & Winguth, C. Transition into a Hothouse World at the Permian-Triassic boundary-A model study. *Palaeogeogr. Palaeoclimatol. Palaeoecol.* **440**, 316–327 (2015).
- Chen, Z. Q. & Benton, M. J. The timing and pattern of biotic recovery following the end-Permian mass extinction. *Nat. Geosci.* **5**, 375–383 (2012).
- Grasby, S. E., Beauchamp, B. & Knies, J. Early Triassic productivity crises delayed recovery from world's worst mass extinction. *Geology* **44**, 779–782 (2016).
- Sun, Y. D. et al. Lethally hot temperatures during the early Triassic greenhouse. *Science* **338**, 366–370 (2012).
- Sedlacek, A. R. C. et al. Sr-87/Sr-86 stratigraphy from the Early Triassic of Zal, Iran: linking temperature to weathering rates and the tempo of ecosystem recovery. *Geology* **42**, 779–782 (2014).
- Song, H. J. et al. Integrated Sr isotope variations and global environmental changes through the late Permian to early late Triassic. *Earth Planet. Sci. Lett.* **424**, 140–147 (2015).

9. Korte, C., Kozur, H. W., Bruckschen, P. & Veizer, J. Strontium isotope evolution of late Permian and Triassic seawater. *Geochim. Cosmochim. Acta* **67**, 47–62 (2003).
10. Algeo, T. J. & Twitchett, R. J. Anomalous early Triassic sediment fluxes due to elevated weathering rates and their biological consequences. *Geology* **38**, 1023–1026 (2010).
11. Midwinter, D., Hadlari, T. & Dewing, K. Lower Triassic river-dominated deltaic successions from the Sverdrup Basin, Canadian Arctic. *Palaeogeogr. Palaeoclimatol. Palaeoecol.* **476**, 55–67 (2017).
12. Retallack, G. J. Postapocalyptic greenhouse paleoclimate revealed by earliest Triassic paleosols in the Sydney Basin, Australia. *Geol. Soc. Am. Bull.* **111**, 52–70 (1999).
13. Sephton, M. A. et al. Catastrophic soil erosion during the end-Permian biotic crisis. *Geology* **33**, 941–944 (2005).
14. Chen, X.-Y., Teng, F.-Z., Huang, K.-J. & Algeo, T. J. Intensified chemical weathering during Early Triassic revealed by magnesium isotopes. *Geochim. Cosmochim. Acta* **287**, 263–276 (2020).
15. Sun, H. et al. Rapid enhancement of chemical weathering recorded by extremely light seawater lithium isotopes at the Permian-Triassic boundary. *Proc. Natl Acad. Sci. USA* **115**, 3782–3787 (2018).
16. Kump, L. R., Brantley, S. L. & Arthur, M. A. Chemical, weathering, atmospheric CO₂, and climate. *Ann. Rev. Earth Planet. Sci.* **28**, 611–667 (2000).
17. Black, B. A. et al. Systemic swings in end-Permian climate from Siberian Traps carbon and sulfur outgassing. *Nat. Geosci.* **11**, 949 (2018).
18. Roaldset, E., Pettersen, E., Longva, O. & Mangerud, J. Remnants of preglacial weathering in western Norway. *Norsk Geologisk Tidsskrift* **62**, 169–178 (1982).
19. Gilg, H. A., Hall, A. M., Ebert, K. & Fallick, A. E. Cool kaolins in Finland. *Palaeogeogr. Palaeoclimatol. Palaeoecol.* **392**, 454–462 (2013).
20. Fredin, O. et al. The inheritance of a Mesozoic landscape in western Scandinavia. *Nat. Commun.* <https://doi.org/10.1038/ncomms14879> (2017).
21. Olesen, O. et al. Deep weathering, neotectonics and strandflat formation in Nordland, northern Norway. *Norsk Geologisk Tidsskrift* **93**, 189–213 (2013).
22. Lidmar-Bergström, K. Relief and saprolites through time on the Baltic Shield. *Geomorphology* **12**, 45–61 (1995).
23. Tan, P., Oberhardt, N., Dypvik, H., Riber, L. & Ferrell, R. E. Jr Weathering profiles and clay mineralogical developments, Bornholm, Denmark. *Mar. Pet. Geol.* **80**, 32–48 (2017).
24. Mørk, M. B. E., Vigran, J. O., Smelror, M., Fjordingstad, V. & Bøe, R. Mesozoic mudstone compositions and the role of kaolinite weathering - a view from shallow cores in the Norwegian Sea (More to Troms). *Nor. J. Geol.* **83**, 61–78 (2003).
25. Sturt, B. A., Dalland, A. & Mitchell, J. L. The age of the sub Mid-Jurassic tropical weathering profile of Andøya, northern Norway, and the implications for the late Palaeozoic palaeogeography in the North Atlantic region. *Geol. Rundsch.* **68**, 523–542 (1979).
26. Dalland, A. The Mesozoic rocks of Andøy, northern Norway. *Norges geologiske undersøkelse Bulletin* **316**, 271–286 (1975).
27. Brønner, M. et al. *Ramså Basin, Northern Norway: An Integrated Study*. Report No. 2017.027, 290 (Geological Survey of Norway, 2017).
28. Smelror, M. Palynostratigraphy & Palynofacies, T. R. Cycles and Palaeoenvironments in the Middle Jurassic–Early Cretaceous Ramså Basin, Northern Norway. *Geosciences* **11**, 354 (2021).
29. Torgersen, E., Viola, G., Zwingmann, H. & Harris, C. Structural and temporal evolution of a reactivated brittle-ductile fault - Part II: timing of fault initiation and reactivation by K-Ar dating of synkinematic illite/muscovite. *Earth Planet. Sci. Lett.* **407**, 221–233 (2014).
30. Viola, G. et al. Deconvoluting complex structural histories archived in brittle fault zones. *Nat. Commun.* <https://doi.org/10.1038/ncomms13448> (2016).
31. Tartaglia, G. et al. “Brittle structural facies” analysis: a diagnostic method to unravel and date multiple slip events of long-lived faults. *Earth Planet. Sci. Lett.* **545**, 116420 (2020).
32. Tsukamoto, S., Tagami, T. & Zwingmann, H. in *Understanding Faults* (eds Tanner, D. & Brandes, C.) Ch. 7 (Elsevier, 2020).
33. Vrolijk, P., Pevear, D., Covey, M. & LaRiviere, A. Fault gouge dating: history and evolution. *Clay Miner.* **53**, 305–324 (2018).
34. Clauer, N., Zwingmann, H., Liewig, N. & Wendling, R. Comparative 40Ar/39Ar and K-Ar dating of illite-type clay minerals: a tentative explanation for age identities and differences. *Earth Sci. Rev.* **115**, 76–96 (2012).
35. Knies, J., Grasby, S. E., Beauchamp, B. & Schubert, C. J. Water mass denitrification during the latest Permian extinction in the Sverdrup Basin, Arctic Canada. *Geology* **41**, 167–170 (2013).
36. Grasby, S. E. et al. Global warming lead to Early Triassic nutrient stress across northern Pangaea. *GSA Bull.* <https://doi.org/10.1130/B32036> (2019).
37. Nesbitt, H. W. & Young, G. M. Early Proterozoic climates and plate motions inferred from major element chemistry. *Nature* **299**, 715–717 (1982).
38. Harnois, L. The CIW index: a new chemical index of weathering. *Sediment. Geol.* **55**, 319–322 (1988).
39. Fedo, C. M., Nesbitt, H. W. & Young, G. M. Unravelling the effects of potassium metasomatism in sedimentary-rocks and paleosols, with implications for paleoweathering conditions and provenance. *Geology* **23**, 921–924 (1995).
40. Parker, A. An index of weathering for silicate rocks. *Geol. Mag.* **107**, 501–504 (1970).
41. Brimhall, G. H. et al. Metal enrichment in bauxites by deposition of chemically mature aeolian dust. *Nature* **333**, 819–824 (1988).
42. Driese, S. G., Medaris, L. G., Ren, M. H., Runkel, A. C. & Langford, R. P. Differentiating pedogenesis from diagenesis in early terrestrial paleoweathering surfaces formed on granitic composition parent materials. *J. Geol.* **115**, 387–406 (2007).
43. Pruett, R. J. & Webb, H. L. Sampling and analysis of KGa-1B well-crystallized kaolin source clay. *Clay Clay Miner.* **41**, 514–519 (1993).
44. Brown, G. & Brindley, G. W. (eds) *Crystal Structure of Clay Minerals and their X-ray Identification* (Mineralogical Society, 1980).
45. Ruiz Cruz M. D. Clay mineral assemblages in flysch from the Campo de Gibraltar area (Spain). *Clay Minerals*, **34**, 345–364 (1999).
46. Nesbitt, H. & Young, G. M. Formation and diagenesis of weathering profiles. *J. Geol.* **97**, 129–147 (1989).
47. Nesbitt, H. W. & Young, G. M. Prediction of some weathering trends of plutonic and volcanic rocks based on thermodynamic and kinetic considerations. *Geochim. Cosmochim. Acta* **48**, 1523–1534 (1984).
48. Sheldon, N. D. & Tabor, N. J. Quantitative paleoenvironmental and paleoclimatic reconstruction using paleosols. *Earth Sci. Rev.* **95**, 1–52 (2009).
49. Vasconcelos, P. M., Renne, P. R., Brimhall, G. H. & Becker, T. A. Direct dating of weathering phenomena by Ar-40/Ar-39 and K-Ar analysis of supergene K-Mn oxides. *Geochim. Cosmochim. Acta* **58**, 1635–1665 (1994).
50. Faure, G. & Mensing, T. M. *Isotopes: Principles and Applications* (Wiley, 2009).
51. Hinckley, D. N. Variability in “crystallinity” values among the kaolin deposits of the coastal plain of Georgia and South Carolina. *Clay Clay Miner.* **11**, 229–235 (1962).
52. Aparicio, P. & Galan, E. Mineralogical interference on kaolinite crystallinity index measurements. *Clays Clay Miner.* **47**, 12–27 (1999).
53. Bauluz, B., Mayayo, M., Yuste, A. & López, J. G. Genesis of kaolinite from Albian sedimentary deposits of the Iberian Range (NE Spain): analysis by XRD, SEM and TEM. *Clay Miner.* **43**, 459–475 (2008).
54. Plançon, A., Giese, R. & Snyder, R. The Hinckley index for kaolinites. *Clay Miner.* **23**, 249–260 (1988).
55. Grathoff, G. H. & Moore, D. Illite polytype quantification using WILDFIRE [C] calculated X-ray diffraction patterns. *Clays Clay Miner.* **44**, 835–842 (1996).
56. Moore, D. M. & Reynolds Jr, R. C. *X-ray Diffraction and the Identification and Analysis of Clay Minerals* 2nd edn (Oxford Univ. Press, 1997).
57. Melo, V., Singh, B., Schaefer, C., Novais, R. & Fontes, M. Chemical and mineralogical properties of kaolinite-rich Brazilian soils. *Soil Sci. Soc. Am. J.* **65**, 1324–1333 (2001).
58. Zwingmann, H. & Mancktelow, N. Timing of Alpine fault gouges. *Earth Planet. Sci. Lett.* **223**, 415–425 (2004).
59. Eide, C. H., Klausen, T. G., Katkov, D., Suslova, A. A. & Helland-Hansen, W. Linking an early Triassic delta to antecedent topography: source-to-sink study of the southwestern Barents Sea margin. *GSA Bull.* **130**, 263–283 (2017).
60. Wignall, P., Morante, R. & Newton, R. The Permo-Triassic transition in Spitsbergen: $\delta^{13}\text{C}_{\text{org}}$ chemostratigraphy, Fe and S geochemistry, facies, fauna and trace fossils. *Geol. Mag.* **135**, 47–62 (1998).
61. Glorstad-Clark, E., Faleide, J. I., Lundschie, B. A. & Nystuen, J. P. Triassic seismic sequence stratigraphy and paleogeography of the western Barents Sea area. *Mar. Petrol. Geol.* **27**, 1448–1475 (2010).
62. Japsen, P., Green, P. F., Chalmers, J. A. & Bonow, J. M. Mountains of southernmost Norway: uplifted Miocene peneplains and re-exposed Mesozoic surfaces. *J. Geol. Soc.* **175**, 721–741 (2018).
63. Migoñ, P. & Lidmar-Bergström, K. Weathering mantles and their significance for geomorphological evolution of central and northern Europe since the Mesozoic. *Earth Sci. Rev.* **56**, 285–324 (2001).
64. Hochuli, P. A. & Vigran, J. O. Climate variations in the Boreal Triassic — Inferred from palynological records from the Barents Sea. *Palaeogeogr. Palaeoclimatol. Palaeoecol.* **290**, 20–42 (2010).
65. Decou, A., Andrews, S. D., Alderton, D. H. M. & Morton, A. Triassic to Early Jurassic climatic trends recorded in the Jameson Land Basin, East Greenland: clay mineralogy, petrography and heavy mineralogy. *Basin Res.* **29**, 658–673 (2017).
66. Korte, C., Jasper, T., Kozur, H. W. & Veizer, J. 87Sr/86Sr record of Permian seawater. *Palaeogeogr. Palaeoclimatol. Palaeoecol.* **240**, 89–107 (2006).
67. Tabor, N. J. Wastelands of tropical Pangea: high heat in the Permian. *Geology* **41**, 623–624 (2013).
68. Wignall, P. B. et al. Volcanism, mass extinction, and carbon isotope fluctuations in the Middle Permian of China. *Science* **324**, 1179–1182 (2009).

69. Zhou, M.-F. et al. A temporal link between the Emeishan large igneous province (SW China) and the end-Guadalupian mass extinction. *Earth Planet. Sci. Lett.* **196**, 113–122 (2002).
70. Guo, F., Fan, W., Wang, Y. & Li, C. When did the Emeishan mantle plume activity start? Geochronological and geochemical evidence from ultramafic dikes in southwestern China. *Int. Geol. Rev.* **46**, 226–234 (2004).
71. Embry, A. & Beauchamp, B. in *Sedimentary Basins of the World* (ed Andrew D. Miall) Ch. 13 (Elsevier, 2008).
72. Altabet, M. A. & Francois, R. Sedimentary nitrogen isotopic ratio as a recorder for surface ocean nitrate utilisation. *Global Biogeochem. Cycles* **8**, 103–116 (1994).
73. Altabet, M. A. et al. The nitrogen isotope biogeochemistry of sinking particles from the margin of the Eastern North Pacific. *Deep Sea Res. I: Oceanogr. Res. Pap.* **46**, 655–679 (1999).
74. Schoepfer, S. D. et al. Termination of a continent-margin upwelling system at the Permian–Triassic boundary (Opal Creek, Alberta, Canada). *Glob. Planet. Change* **105**, 21–35 (2013).
75. Williams, L. B. et al. Nitrogen isotope geochemistry of organic matter and minerals during diagenesis and hydrocarbon migration. *Geochim. Cosmochim. Acta* **59**, 765–779 (1995).
76. Ader, M., Boudou, J.-P., Javoy, M., Goffé, B. & Daniels, E. Isotope study on organic nitrogen of Westphalian anthracites from the Western Middle field of Pennsylvania (USA) and from the Bramsche Massif (Germany). *Org. Geochem.* **29**, 315–323 (1998).
77. Wada, E. & Hattori, A. Natural abundance of ^{15}N in particulate organic matter in the North Pacific Ocean. *Geochim. Cosmochim. Acta* **40**, 249–251 (1976).
78. Karl, D. et al. in *The Nitrogen Cycle at Regional to Global Scales* (Springer, 2002).
79. Grasby, S. E., Beauchamp, B., Embry, A. & Sanei, H. Recurrent Early Triassic ocean anoxia. *Geology* **41**, 175–178 (2013).
80. Algeo, T. J., Chen, Z. Q., Fraiser, M. L. & Twitchett, R. J. Terrestrial–marine teleconnections in the collapse and rebuilding of Early Triassic marine ecosystems. *Palaeogeogr. Palaeoclimatol. Palaeoecol.* **308**, 1–11 (2011).
81. Japsen, P., Green, P. F., Bonow, J. M. & Erlstrom, M. Episodic burial and exhumation of the southern Baltic Shield: Epeirogenic uplifts during and after break-up of Pangaea. *Gondwana Res.* **35**, 357–377 (2016).
82. Winguth, C. & Winguth, A. M. E. Simulating Permian–Triassic oceanic anoxia distribution: Implications for species extinction and recovery. *Geology* **40**, 127–130 (2012).
83. Meyer, K. M., Yu, M., Jost, A. B., Kelley, B. M. & Payne, J. L. delta C-13 evidence that high primary productivity delayed recovery from end-Permian mass extinction. *Earth Planet. Sci. Lett.* **302**, 378–384 (2011).
84. Meyer, K. M., Kump, L. R. & Ridgwell, A. Biogeochemical controls on photic-zone euxinia during the end-Permian mass extinction. *Geology* **36**, 747–750 (2008).
85. Hotinski, R. M., Bice, K. L., Kump, L. R., Najjar, R. G. & Arthur, M. A. Ocean stagnation and end-Permian anoxia. *Geology* **29**, 7–10 (2001).
86. Corfu, F. U-Pb age, setting and tectonic significance of the anorthosite-mangerite-charnockite-granite suite, Lofoten-Vesteralen, Norway. *J. Petrol.* **45**, 1799–1819 (2004).
87. Vogt, C., Lauterjung, J. & Fischer, R. X. Investigation of the clay fraction (<math> < \mu\text{m}</math>) of the Clay Minerals Society reference clays. *Clay Clay Miner.* **50**, 388–400 (2002).
88. Warr, L. N. A new collection of clay mineral ‘Crystallinity’ Index standards and revised guidelines for the calibration of Kübler and Árkai indices. *Clay Miner.* **53**, 339–350 (2018).
89. Warr, L. & Rice, A. Interlaboratory standardization and calibration of clay mineral crystallinity and crystallite size data. *J. Metamorph. Geol.* **12**, 141–152 (1994).
90. Jochum, K. P. et al. Determination of reference values for NIST SRM 610–617 glasses following ISO guidelines. *Geostand. Geoanal. Res.* **35**, 397–429 (2011).
91. McDougall, I. & Roksandic, Z. Total fusion $^{40}\text{Ar}/^{39}\text{Ar}$ ages using HIFAR reactor. *J. Geol. Soc. Aust.* **21**, 81–89 (1974).
92. Lippolt, H. & Hess, J. HD-B1-biotite reference material for K–Ar chronometry. *Int. J. Rad. Appl. Instrum. D.* **17**, 436–437 (1990).
93. Charbit, S., Guillou, H. & Turpin, L. Cross calibration of K–Ar standard minerals using an unspiked Ar measurement technique. *Chem. Geol.* **150**, 147–159 (1998).
94. McDougall, I. & Wellman, P. Calibration of GA1550 biotite standard for K/Ar and $^{40}\text{Ar}/^{39}\text{Ar}$ dating. *Chem. Geol.* **280**, 19–25 (2011).
95. Steiger, R. H. & Jäger, E. Subcommittee on geochronology; convention on the use of decay constants in geo- and cosmochronology. *Earth Planet. Sci. Lett.* **36**, 359–362 (1977).
96. Schubert, C. J. & Calvert, S. E. Nitrogen and carbon isotopic composition of marine and terrestrial organic matter in Arctic Ocean sediments: implications for nutrient utilization and organic matter composition. *Deep Sea Res. I: Oceanogr. Res. Pap.* **48**, 789–810 (2001).
97. Scotese, C. R. A continental drift flipbook. *J. Geol.* **112**, 729–741 (2004).
98. Bøe, R., Fossen, H. & Smelror, M. Mesozoic sediments and structures onshore Norway and in the coastal zone. *Norg. Geol. Unders. B.* **450**, 15–32 (2010).
99. Royer, D. L. CO_2 -forced climate thresholds during the Phanerozoic. *Geochim. Cosmochim. Acta* **70**, 5665–5675 (2006).
100. Torsvik, T. H., Carlos, D., Mosar, J., Cocks, L. R. M. & Malme, T.N. In *BATLAS - Mid Norway Plate Reconstruction Atlas with Global and Atlantic Perspectives* Ch. 2 (ed. Eide, E. A.) (NGU, 2002).

Acknowledgements

We thank the Norwegian Petroleum Directorate for accessing the offshore borehole material. We are grateful to Atle Mørk for supporting the sample party. We acknowledge Andrew Todd (CSIRO) and Ruikai Xie (NGU) for the K–Ar geochronological work. The research is funded by the Research Council of Norway (grants #319849 and #223259).

Author contributions

The main idea was developed by J.K., G.V., M.B., and O.F. J.K., G.V., and H.Z. wrote most of the text. XRD analyses were conducted by C.V., J.S., and H.Z. K–Ar geochronology was established by H.Z. and R.v.d.L. SEM–CL data were provided by A.M. The regional geology was described by M.S. and S.E.G. and B.B. provided data from Sverdrup Basin. P.E.V. provided the TEM analyses. All authors discussed the results and commented on the manuscript.

Funding

Open access funding provided by UiT The Arctic University of Norway (incl University Hospital of North Norway).

Competing interests

The authors declare no competing interests.

Additional information

Supplementary information The online version contains supplementary material available at <https://doi.org/10.1038/s43247-022-00480-z>.

Correspondence and requests for materials should be addressed to Jochen Knies.

Peer review information *Communications Earth & Environment* thanks Eva Elisabeth Stueeken and the other, anonymous, reviewer(s) for their contribution to the peer review of this work. Primary Handling Editors: Mojtaba Fakhraee, Joe Aslin, Clare Davis.

Reprints and permission information is available at <http://www.nature.com/reprints>

Publisher’s note Springer Nature remains neutral with regard to jurisdictional claims in published maps and institutional affiliations.



Open Access This article is licensed under a Creative Commons Attribution 4.0 International License, which permits use, sharing, adaptation, distribution and reproduction in any medium or format, as long as you give appropriate credit to the original author(s) and the source, provide a link to the Creative Commons license, and indicate if changes were made. The images or other third party material in this article are included in the article’s Creative Commons license, unless indicated otherwise in a credit line to the material. If material is not included in the article’s Creative Commons license and your intended use is not permitted by statutory regulation or exceeds the permitted use, you will need to obtain permission directly from the copyright holder. To view a copy of this license, visit <http://creativecommons.org/licenses/by/4.0/>.

© The Author(s) 2022